

Dam break of viscoplastic elliptical objects

Kindness Isukwem* and Anselmo Pereira†

Mines Paris, PSL University, Centre for material forming (CEMEF),
UMR CNRS 7635, rue Claude Daunesse, 06904 Sophia-Antipolis, France

(Dated: October 7, 2024)

In this note, we numerically and theoretically analyze the physical mechanisms controlling the gravity-induced spreading of viscoplastic elliptical metric objects on a sticky solid surface (without sliding). The two-dimensional collapsing objects are described as Bingham fluids. The numerical simulations are based on a variational multi-scale approach devoted to multiphase non-Newtonian fluid flows. The results are depicted by considering the spreading dynamics, energy budgets, and new scaling laws. They show that, under negligible inertial effects, the driving gravitational energy of the elliptical columns is dissipated through viscoplastic effects during the collapse, giving rise to three flow regimes: gravito-viscous, gravito-plastic, and mixed gravito-visco-plastic. These regimes are strongly affected by the initial aspect ratio of the collapsing column, which reveals the possibility of using morphology to control spreading. Finally, the results are summarized in a diagram linking the object's maximum spreading and the collapse time with different collapsing regimes through a single dimensionless parameter called *collapse number*.

Keywords: gravity-driven spreading; multiphase non-Newtonian fluid flow; Bingham fluid; spreading dynamics; scaling laws.

I. INTRODUCTION

The gravitational collapse of a complex fluid column is a paramount topic in Fluid Mechanics [1, 2]. It is related to a wide range of natural and applicative issues, from geophysical to industrial contexts, which includes preventing disasters caused by mud surges and the sudden collapse of mine tailing deposits, and controlling the release of fluids in non-conventional rheometric tests, such as the slump test for concrete and the Bostwick test for food [3–6]. In such flow scenarios, many complex fluids behave as ideal (non-deformable) solids at low-stress levels and non-Newtonian liquids at stress levels above their yield stress τ_0 , thus termed viscoplastic fluids [7]. Definitively, micro-structural interactions developed in these fluids (such as intermolecular attractive/repulsive forces, friction, capillary bridge, etc.) are translated macroscopically through a yield stress and a strain-rate-dependent viscosity η . This viscosity is often represented by the Bingham equation as $\eta = k + \tau_0/|\dot{\gamma}|$, where k is the consistency index and $|\dot{\gamma}|$ is the norm of the strain-rate tensor [8, 9]. Most fluids have been seen to behave like viscoplastic fluids under certain flow conditions. They include mineral suspensions (bentonite, kaolin, carbon black, etc.), organic suspensions/gels (Carbopol, alginate, ketchup, etc.), emulsions (mayonnaise) and foams [10–12].

Gravity-induced flows of viscoplastic fluid columns can be substantially affected by τ_0 [1, 2, 13]. When sufficiently high, the yield stress can hold the fluid up against gravity, either preventing the onset of the collapse or

stopping the fluid flow due to the development of localised rigid-like regions commonly named *plugs* [2]. Interestingly, the growth of such regions is highly affected by morphological aspects of the fluid column, a topic scarcely explored in the literature, which has mainly focused on cylinders and prisms [1, 2]. Hence, it is reasonable to extend these studies to include other morphologies, for example, objects that can be considered two-dimensional (objects whose width \gg height and thickness, for instance). In that sense, one key question is: can we predict the maximum spreading reached by a collapsing viscoplastic 2D column under gravity effects and the spreading time? We provide an answer to this question in the present work.

In this short communication, we present a theoretical and numerical study devoted to the physical mechanisms driving the gravity-induced collapse of viscoplastic elliptical objects on a sticky solid surface. More specifically, we extend previous cylindrical and prismatic-based works [1, 2] by analyzing the spreading dynamics, maximum spreading, and spreading time of viscoplastic elliptical columns (2D). We employ 2D numerical simulations based on a variational multi-scale approach devoted to non-Newtonian multiphase flows. The results are analyzed by considering the spreading dynamics, energy budgets, and new scaling laws. Lastly, they are summarized in a two-dimensional diagram linking the maximum spreading and its spreading time with different flow regimes through a single dimensionless parameter called here the *collapse number*.

The organisation of the paper is as follows. A detailed description of the physical formulation and the numerical method is presented in section II. Numerical results are discussed in section III. Finally, conclusions and perspectives are drawn in the closing section.

* kindness-chinwendu.isukwem@minesparis.psl.eu

† anselmo.soeiro_pereira@minesparis.psl.eu

II. PHYSICAL FORMULATION, NUMERICAL METHOD AND DIMENSIONLESS NUMBERS

As previously mentioned, we study the spreading of viscoplastic elliptical objects with metric dimensions on a no-slip solid surface, as depicted in figure 1. These objects, characterized by an initial height H_0 , thickness D_0 , density ρ , consistency k , and yield stress τ_0 , collapse under the influence of gravity \mathbf{g} . Following the collapse, they spread slowly across the solid surface as their gravitational potential energy is dissipated through viscoplastic effects. The collapse continues until the objects reach a maximum spreading D_{max} and a minimum height H_{min} at time t_c . Figure 1 illustrates the spreading at four different times, ranging from $t/t_c = 0$ (onset of collapse) to $t/t_c = 1$ (stoppage). The 2D objects and the solid surface are surrounded by air, which has a density ρ_{air} and viscosity η_{air} .

Our computational method is based on a massively parallel finite element library (CIMLIB-CFD) devoted to non-Newtonian multiphase flows [2, 12, 14–19]. More specifically, we apply the momentum conservation equation presented below to the solenoidal flow ($\nabla \cdot \mathbf{u} = 0$) described earlier (figure 1):

$$\rho \left(\frac{\partial \mathbf{u}}{\partial t} + \mathbf{u} \cdot \nabla \mathbf{u} - \mathbf{g} \right) = -\nabla p + \nabla \cdot \boldsymbol{\tau}, \quad (1)$$

where \mathbf{u} is the velocity vector, ∇ denotes the gradient operator, \mathbf{g} represents the gravitational acceleration vector, p is the pressure, and $\boldsymbol{\tau}$ is the extra-stress tensor. The extra-stress tensor is defined as $\boldsymbol{\tau} = \eta \dot{\boldsymbol{\gamma}}$, where $\dot{\boldsymbol{\gamma}}$ represents the rate-of-strain tensor, given by $\dot{\boldsymbol{\gamma}} = (\nabla \mathbf{u} + \nabla \mathbf{u}^T)$. Our 2D objects are modelled as Bingham fluids, with viscosity η described by:

$$\eta = k + \frac{\tau_0}{|\dot{\boldsymbol{\gamma}}|} \left(1 - e^{-|\dot{\boldsymbol{\gamma}}|/\dot{\gamma}_p} \right). \quad (2)$$

As indicated in equation 2, the viscosity incorporates the Papanastasiou regularization term, shown in parentheses, which prevents numerical divergence when the norm of the rate-of-strain tensor, $|\dot{\boldsymbol{\gamma}}|$, approaches zero [20]. This regularization ensures that the viscosity plateaus when $|\dot{\boldsymbol{\gamma}}|$ falls below $\dot{\gamma}_p$, where $\dot{\gamma}_p = 10^{-6} \text{s}^{-1}$.

The numerical methods used here are based on a *Variational Multiscale Method* (VMS) coupled with an anisotropic mesh adaptation method [2, 12, 14–19]. The meshes used are composed of approximately 10^5 elements whose minimum size is $1 \mu\text{m}$ (see the black lines in figure 1). The time-dependent evolution of the 2D object's interface is captured using a Level-Set function. It is important to emphasise that our numerical multi-phase framework has been validated for a variety of flow scenarios, which includes the impact of drops [12, 17–19], dam breaks [2], the stretching and breakup of filaments [14], and the development of buckling instabilities [15, 16] using Newtonian and non-Newtonian fluids.

The 2D collapsing objects are on a metric scale of $H_0 = 1\text{m}$, and the aspect ratios of H_0/D_0 range from

0.25 to 10. Gravity $|\mathbf{g}| = 1000\text{m/s}^2$. A yield-stress spectrum ranging from 10^{-5}Pa to 0.4Pa is considered, while the consistency and the density of the elliptical columns are held constant at $k = 1\text{Pa}\cdot\text{s}$ and $\rho = 10^{-3}\text{kg/m}^3$, respectively. The viscosity and density of the surrounding air are set at $\eta_{air} = 10^{-5}\text{Pa}\cdot\text{s}$ and $\rho_{air} = 1\text{kg/m}^3$. Additionally, a no-slip condition is imposed between the collapsing objects and the solid surface, with zero normal stresses on the walls of the computational domain [similar to 2]. A movie showing a typical numerical simulation is available in which $H_0 = 1\text{m}$, $D_0 = 0.5\text{m}$, $\rho = 0.001\text{kg/m}^3$, $k = 1\text{Pa}\cdot\text{s}$, $\tau_0 = 0.38\text{Pa}$, $|\mathbf{g}| = 1000\text{m/s}^2$ (the colors indicate the norm of the velocity vector $|\mathbf{u}|$). (<https://youtu.be/aCiPFHAMWBE>)

The dimensionless numbers that govern the problem denoted as Π_i , are derived from the Buckingham-II theorem. The relevant variables considered are H_0 , D_0 , ρ , k , τ_0 , \mathbf{g} and the characteristic collapse velocity U_c (which will be deduced in the following lines). The fundamental units involved are mass [kg], length [m], and time [s]. This analysis leads to four significant dimensionless quantities:

$$\Pi_1 = \frac{H_0}{D_0}, \quad (3)$$

$$\Pi_2 = \frac{k(U_c/D_0)}{\rho g H_0}, \quad (4)$$

$$\Pi_3 = \frac{\tau_0}{\rho g H_0}, \quad (5)$$

$$\Pi_4 = \frac{\rho U_c^2}{\rho g H_0}, \quad (6)$$

where $\Pi_2 = 1/\text{Ga}_k$ (Ga_k is the k -based Galileo number), $\Pi_3 = \text{Pl}$ (Pl is the plastic number) and $\Pi_4 = \text{Fr}$ (Fr is the Froude number). Given that the flows considered here are inertia-free (this will be shown in detail in Section III through energy budgets), ρU_c^2 is negligible when compared to the gravitational stress $\rho g H_0$ (typically $\Pi_4 \lesssim 10^{-5}$). Consequently, our flow scenarios can be described with the aid of three dimensionless numbers:

$$\frac{H_0}{D_0} \quad (\text{aspect ratio}), \quad (7)$$

$$1/\text{Ga}_k = \frac{k(U_c/D_0)}{\rho g H_0} \quad (\text{inverse Galileo number}), \quad (8)$$

$$\text{Pl} = \frac{\tau_0}{\rho g H_0} \quad (\text{plastic number}). \quad (9)$$

The impact of these three dimensionless numbers on the collapse of viscoplastic 2D columns is examined in section III. Specifically, the results are framed and analyzed in terms of these dimensionless parameters, providing a clear understanding of how each one influences the spreading dynamics.

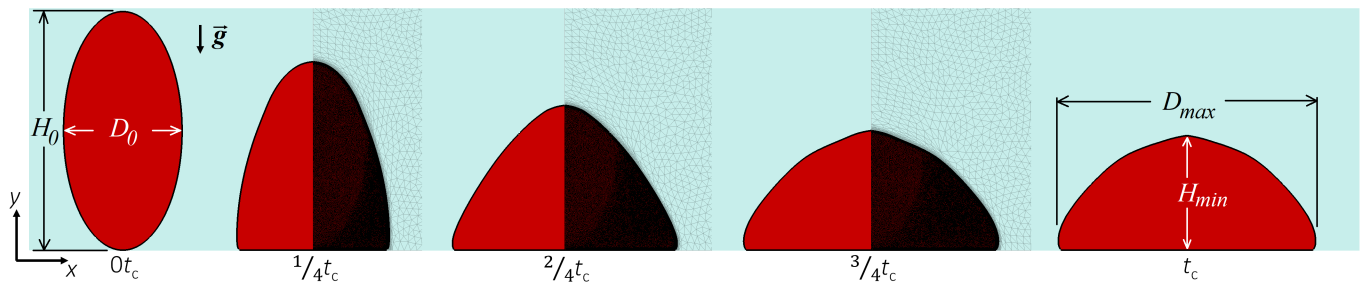


FIG. 1. Multiphase numerical simulation: a typical collapse and spreading of a viscoplastic elliptical object (shown in red) of initial height H_0 , initial thickness D_0 , density ρ , consistency k , and yield stress τ_0 on a sticky surface. After the onset of the collapse at time t_0 , the object spreads until it reaches its maximum spreading D_{max} and a minimum height H_{min} at time t_c . Both the 2D object and the solid surface are surrounded by air (depicted in blue). The mesh used in the simulation, shown with black and gray lines, consists of approximately 10^5 elements, with a minimum size of $1\mu\text{m}$. A movie showing a typical numerical simulation is available in which $H_0 = 1\text{m}$, $D_0 = 0.5\text{m}$, $\rho = 0.001\text{kg/m}^3$, $k = 1\text{Pa}\cdot\text{s}$, $\tau_0 = 0.38\text{Pa}$, $|g| = 1000\text{m/s}^2$ (the colors indicate the norm of the velocity vector $|\mathbf{u}|$). (<https://youtu.be/aCiPFHAMWBE>)

Finally, a characteristic collapse velocity, U_c , can be defined by considering that the gravitational energy (per unit length) of the elliptical fluid object at $t = 0\text{s}$ ($\rho g H_0 \frac{\pi H_0 D_0}{4}$) is converted into kinetic energy [$\frac{\rho U_c^2}{2} \frac{\pi H_0 D_0}{4}$], and dissipated [$4k \frac{U_c}{H_0} H_0 D_0 + 2\tau_0 H_0 D_0$, from the column compression standpoint] throughout the collapse process. The factors 4 and 2 in the viscous and plastic dissipation terms account for the planar compression along the 2D column, which will be further illuminated in section III. This yields the following equation:

$$\frac{\pi}{4} \frac{\rho}{2} U_c^2 + \frac{4k}{H_0} U_c - \left(\rho g H_0 \frac{\pi}{4} - 2\tau_0 \right) = 0, \quad (10)$$

which can be solved for the collapse velocity U_c

$$U_c = \frac{-\frac{4k}{H_0} + \sqrt{\left(\frac{4k}{H_0}\right)^2 + \frac{\pi\rho}{2} (\rho g H_0 \frac{\pi}{4} - 2\tau_0)}}{\frac{\pi\rho}{4}}. \quad (11)$$

This equation is used in computing $1/\text{Ga}_k$. By rearranging equation 10, we find:

$$1 = \frac{1}{2}\text{Fr} + \frac{16}{\pi} \frac{1}{\text{Ga}_k} + \frac{8}{\pi}\text{Pl}, \quad (12)$$

where the first term on right-hand side is denoted as Π_{Fr} , the second term as Π_{Ga_k} , and the last term as Π_{Pl} . Notably, Π_{Fr} , Π_{Ga_k} and Π_{Pl} are bounded between 0 and 1. However, for the flow cases analyzed here, $\Pi_{\text{Fr}} \approx 0$. Equation 12 becomes then

$$1 = \frac{16}{\pi} \frac{1}{\text{Ga}_k} + \frac{8}{\pi}\text{Pl}. \quad (13)$$

When $\tau_0 = 0\text{Pa}$, $\Pi_{\text{Ga}} = 1$. On the other hand, a fully plastic case occurs at $\Pi_{\text{Pl}} = 1$, indicating ultimately that fluid column behaves as a non-deformable solid (e.g., absence of flow).

III. RESULTS AND DISCUSSION

Figure 2 shows the gravity-induced collapse of elliptical objects whose $H_0/D_0 = 2$, following their spreading over a solid surface at three different Pl/Ga_k pairs: $\text{Pl} = 0.05$, $1/\text{Ga}_k = 0.171$ (sub-figure 2a); $\text{Pl} = 0.3$, $1/\text{Ga}_k = 0.046$ (sub-figure 2b); and $\text{Pl} = 0.35$, $1/\text{Ga}_k = 0.021$ (sub-figure 2c). Each sub-figure is composed of six snapshots illustrating the spreading at six different instants, from the onset ($t/t_c = 0$) to stoppage ($t/t_c = 1$). These images highlight not only the instantaneous morphology of the objects but also the contours of the deformation rate $|\dot{\gamma}|$ (made dimensionless by U_c/H_0) on the left, together with the unyielded regions ($|\boldsymbol{\tau}| \leq \tau_0$; black areas behaving like an ideal solid) and the yielded regions ($|\boldsymbol{\tau}| > \tau_0$; gray areas behaving like a non-Newtonian liquid) on the right.

As shown by comparing sub-figures 2(a), 2(b), and 2(c), the increase in plastic number Pl (conversely a decrease in $1/\text{Ga}_k$, see equation 13) accentuates yield stress relative to the gravitational stress, resulting in lesser relative spreading D_{max}/D_0 . Additionally, the increase in Pl favors the development of unyielded regions (in black), especially in areas of the 2D objects far from the solid surface, where the deformation rate is minimal. It is also worth noting that the most significant values of $|\dot{\gamma}|/(U_c/H_0)$ primarily develop within a layer whose thickness is comparable to H_{min} , as indicated by the magenta dotted lines. In other words, H_{min} corresponds to the thickness of the layer in the non-Newtonian fluid where the energy dissipation mechanism is predominantly active.

The influence of H_0/D_0 on the collapse process is highlighted in figure 3, where the instantaneous relative spreading $D(t)/D_0$ is plotted as a function of t/t_c at three different aspect ratios: $H_0/D_0 = 2$ (sub-figure 3a), $H_0/D_0 = 6$ (sub-figure 3b), and $H_0/D_0 = 10$ (sub-figure 3a). Moving downwards on each sub-plot denotes increasing Pl across seven values represented by distinct symbols (as indicated by the magenta arrows):

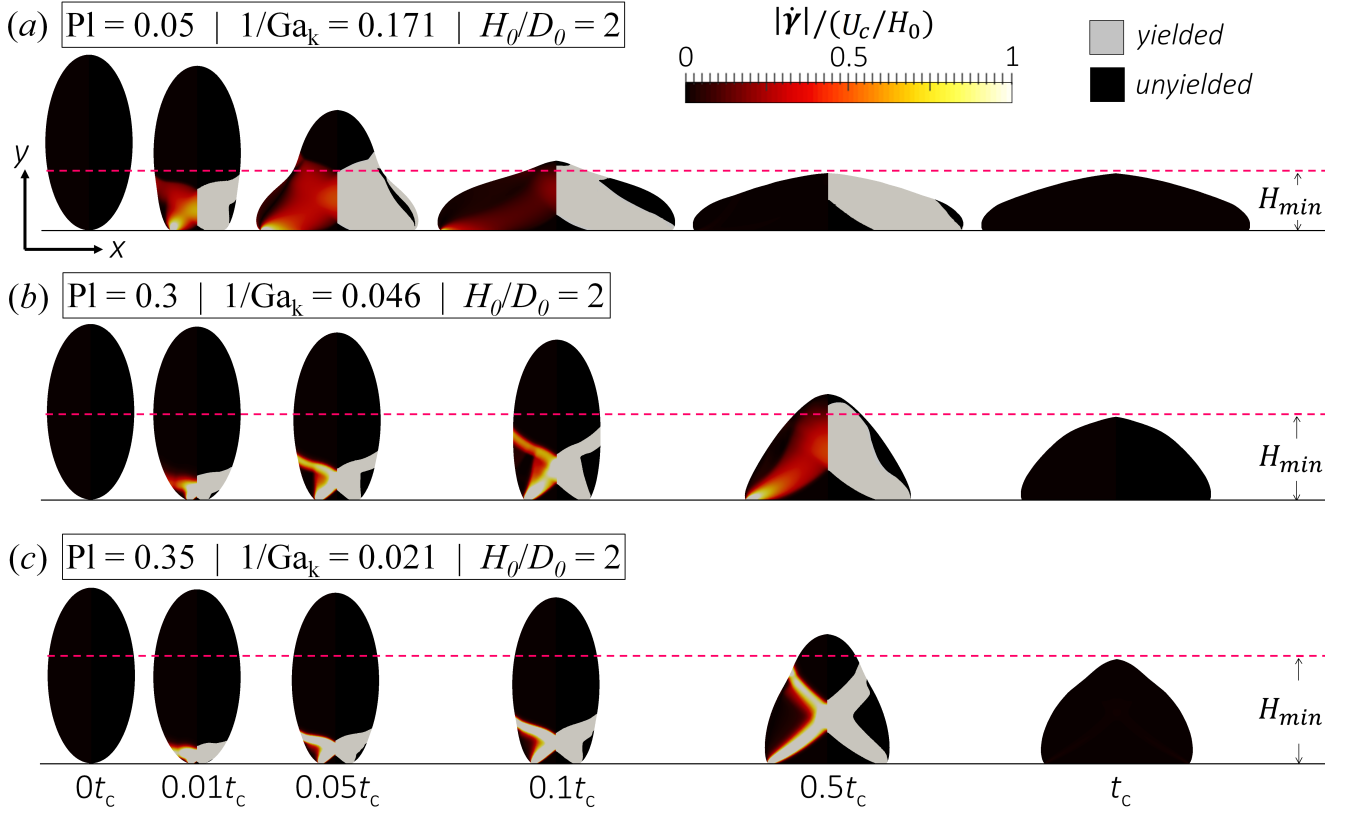


FIG. 2. Spreading of elliptical objects with $H_0/D_0 = 2$, following their collapse over a solid surface for three different PI - $1/Ga_k$ pairs: (a) $PI = 0.05$, $1/Ga_k = 0.171$; (b) $PI = 0.3$, $1/Ga_k = 0.046$; (c) and $PI = 0.35$, $1/Ga_k = 0.021$. Each sub-figure is composed of six images illustrating the spreading of the object at six different times, from onset ($t/t_c = 0$) to stoppage ($t/t_c = 1$). These images also highlight the contours of the deformation rate $|\dot{\gamma}|$ (made dimensionless by U_c/H_0) on the left, together with the unyielded regions ($|\tau| \leq \tau_0$; black areas behaving like an ideal solid) and the yielded regions ($|\tau| > \tau_0$; gray areas behaving like a non-Newtonian liquid) on the right.

$PI = 0.0001$ (gray circles), $PI = 0.001$ (blue triangles), $PI = 0.005$ (red diamonds), $PI = 0.01$ (orange inverted triangles), $PI = 0.05$ (green squares), $PI = 0.1$ (cyan crosses), and $PI = 0.3$ (black asterisks), which results in lesser relative spreading as previously discussed. As observed by confronting sub-figures 3(a), 3(b), and 3(c), $D(t)/D_0$ increases with H_0/D_0 , a direct consequence of the augmentation of unyielded regions at the top part of the elliptical objects, ultimately causing deformation to be concentrated in regions closer to the solid surface. Similar trends are seen in elliptical (2D) and prolate (3D) impacting objects [12, 17, 19].

To gain deeper insight into the physical mechanisms governing the spreading process, we examine the energy transfer during the collapse of viscoplastic elliptical objects, as illustrated in figure 4. The energy percentage curves are plotted against dimensionless time, illustrating the gravitational energy G , kinetic energy KE , and dissipated energy W . These energy terms (per unit width) are defined as follows:

$$G = \int_S \rho g y dS, \quad (14)$$

$$KE = \int_S \frac{\rho |\mathbf{u}|^2}{2} dS, \quad (15)$$

$$W = \int_t \int_S \left(\frac{k}{2} |\dot{\gamma}| + \tau_0 \right) |\dot{\gamma}| dS dt, \quad (16)$$

where S denotes the surface of the ellipses. The dissipated energy (per unit width) is made up of its viscous contributions $W_v = \int_t \int_S \frac{k}{2} |\dot{\gamma}|^2 dS dt$ and yield-stress-based contributions $W_{\tau_0} = \int_t \int_S \tau_0 |\dot{\gamma}| dS dt$. Moreover, the dissipated energy can be divided into three components: $W_u = \int_t \int_S \frac{k}{2} \frac{\dot{\gamma}_{yy}^2}{2} + \tau_0 \frac{\dot{\gamma}_{yy}^2}{2|\dot{\gamma}|} dS dt$ related to the planar compression on the wall-normal (y) direction, $W_b = \int_t \int_S \frac{k}{2} \frac{\dot{\gamma}_{xx}^2}{2} + \tau_0 \frac{\dot{\gamma}_{xx}^2}{2|\dot{\gamma}|} dS dt$ associated to the planar expansion in the spreading (x) direction, and the complementary shear-based part $W_s = W - (W_u + W_b)$ (where $\dot{\gamma}_{xx} = 2\partial u_x/\partial x$, and $\dot{\gamma}_{yy} = 2\partial u_y/\partial y$). Each energy term is normalized by the total system energy $E_0 = G(t=0)$: $G^* = G/E_0 \times 100[\%]$ (gray circles), $KE^* = KE/E_0 \times 100[\%]$ (blue triangles), $W^* = W/E_0 \times 100[\%]$ (red diamonds), $W_v^* = W_v/E_0 \times 100[\%]$ (orange inverted triangles), $W_{\tau_0}^* = W_{\tau_0}/E_0 \times 100[\%]$ (green squares),

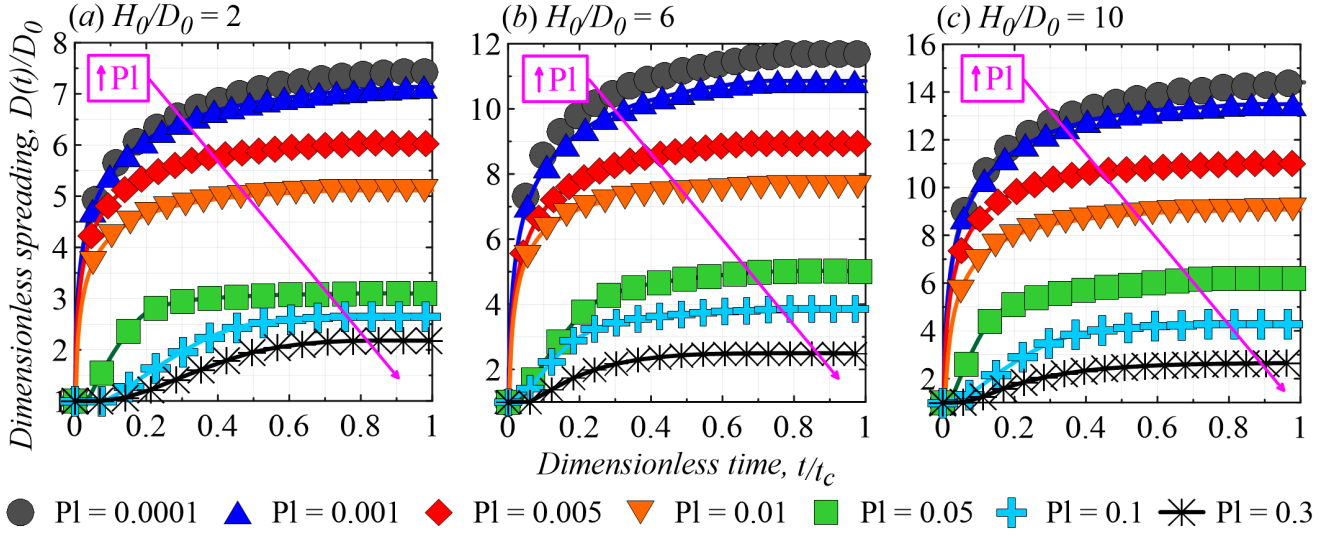


FIG. 3. Instantaneous relative spreading $D(t)/D_0$ as a function of t/t_c to highlight the effect of the aspect ratio: (a) $H_0/D_0 = 2$, (b) $H_0/D_0 = 6$, and (c) $H_0/D_0 = 10$. Seven PI values are considered in each sub-figure: PI = 0.0001 (gray circles), PI = 0.001 (blue triangles), PI = 0.005 (red diamonds), PI = 0.01 (orange inverted triangles), PI = 0.05 (green squares), PI = 0.1 (cyan crosses), and PI = 0.3 (black asterisks). Moving downwards on each sub-plot denotes increasing PI (indicated by the magenta arrows).

$W_u^* = W_u/E_0 \times 100[\%]$ (magenta stars), $W_b^* = W_b/E_0 \times 100[\%]$ (cyan crosses), and $W_s^* = W_s/E_0 \times 100[\%]$ (black asterisks). Moreover, each sub-figure corresponds to a specific PI- $1/Ga_k$ pair at $H_0/D_0 = 2$: (a) PI = 0.005 and $1/Ga_k = 0.19$; (b) PI = 0.05 and $1/Ga_k = 0.17$; and (c) PI = 0.3 and $1/Ga_k = 0.046$.

For all cases presented in figure 4 the object's spreading is initiated by its initial gravitational energy, $G^*(t=0) = 100\%$, which is dominantly dissipated by viscoplastic effects, with a negligible part converted into kinetic energy (as anticipated in section II). At PI = 0.005 and $1/Ga_k = 0.19$ (sub-figure 4a), G^* is mainly dissipated by viscous effects W_v^* , indicating that the collapse and subsequent spreading is governed by the interplay between gravitational and viscous stresses, characteristic of a gravito-viscous regime. As PI increases (and consequently $1/Ga_k$ decreases), the yield-stress contribution to the dissipation W_{τ_0} becomes significant (sub-figure 4b), eventually becoming the dominant dissipation mechanism in the spreading (sub-figure 4c). In this gravito-plastic regime, the object's deformation is driven by the competition between gravitational and yield-stress effects.

Focusing on the dissipation terms displayed in figure 4, it is essential to note that W_u^* , W_b^* and W_s^* are comparable in magnitude in all flow regimes (although in the gravito-viscous scenario, the shear component is slightly lower). Expressed differently, the 2D dam breaks explored here undergo a complex dissipative process emerging from equivalent planar compression/expansion-based and shear-based contributions.

The energy balances depicted in figure 4 reveal the presence of at least two distinct collapse regimes: the gravito-viscous regime (sub-figure 4a); and the gravito-plastic regime (figure 4c). In the gravito-viscous regime,

the gravitational energy (per unit width) of 2D objects at collapse [$\sim \rho g H_0 (H_0 D_0)$] is primarily dissipated by viscous effects. Since $W_u^* \approx W_b^* \approx W_s^*$ as shown in figure 4, we choose to define the dissipated energy in the gravito-viscous regime based on a shear perspective [$\sim k \left(\frac{U_c}{H_{min}}\right) D_{max}^2$, where H_{min} is taken as the dissipative length scale, following the deformation rate contours pointed out by figure 2]. In the gravito-plastic regime, the gravitational energy (per unit width) is dissipated by yield-stress effects ($\sim \tau_0 D_{max}^2$). By equating these energy terms and considering that $H_{min} \sim H_0 D_0 / D_{max}$ based on the principle of mass conservation, we can derive the following results:

$$\frac{D_{max}}{D_0} \sim \left(Ga_k \frac{H_0}{D_0} \right)^{1/3} \quad (\text{gravito-viscous collapse}), \quad (17)$$

$$\frac{D_{max}}{D_0} \sim \left(\frac{1}{PI} \frac{H_0}{D_0} \right)^{1/2} \quad (\text{gravito-plastic collapse}). \quad (18)$$

The transition between these two regimes can be determined by equating equations 17 and 18, leading to the expression $(\frac{1}{PI})^{1/2} \left(\frac{1}{Ga_k}\right)^{1/3} \left(\frac{H_0}{D_0}\right)^{1/6} \sim 1$. This dimensionless quantity is referred to as the *collapse number*, denoted as $Co = (\frac{1}{PI})^{1/2} \left(\frac{1}{Ga_k}\right)^{1/3} \left(\frac{H_0}{D_0}\right)^{1/6}$. When $Co \sim 1$, the transition between the gravito-viscous and gravito-plastic regimes is expected to occur.

The theoretical argument stressed above is supported by the data shown in sub-figure 5(a), where the rescaled maximum spreading $\frac{D_{max}/D_0}{(Ga_k H_0/D_0)^{1/3}}$, is plotted against

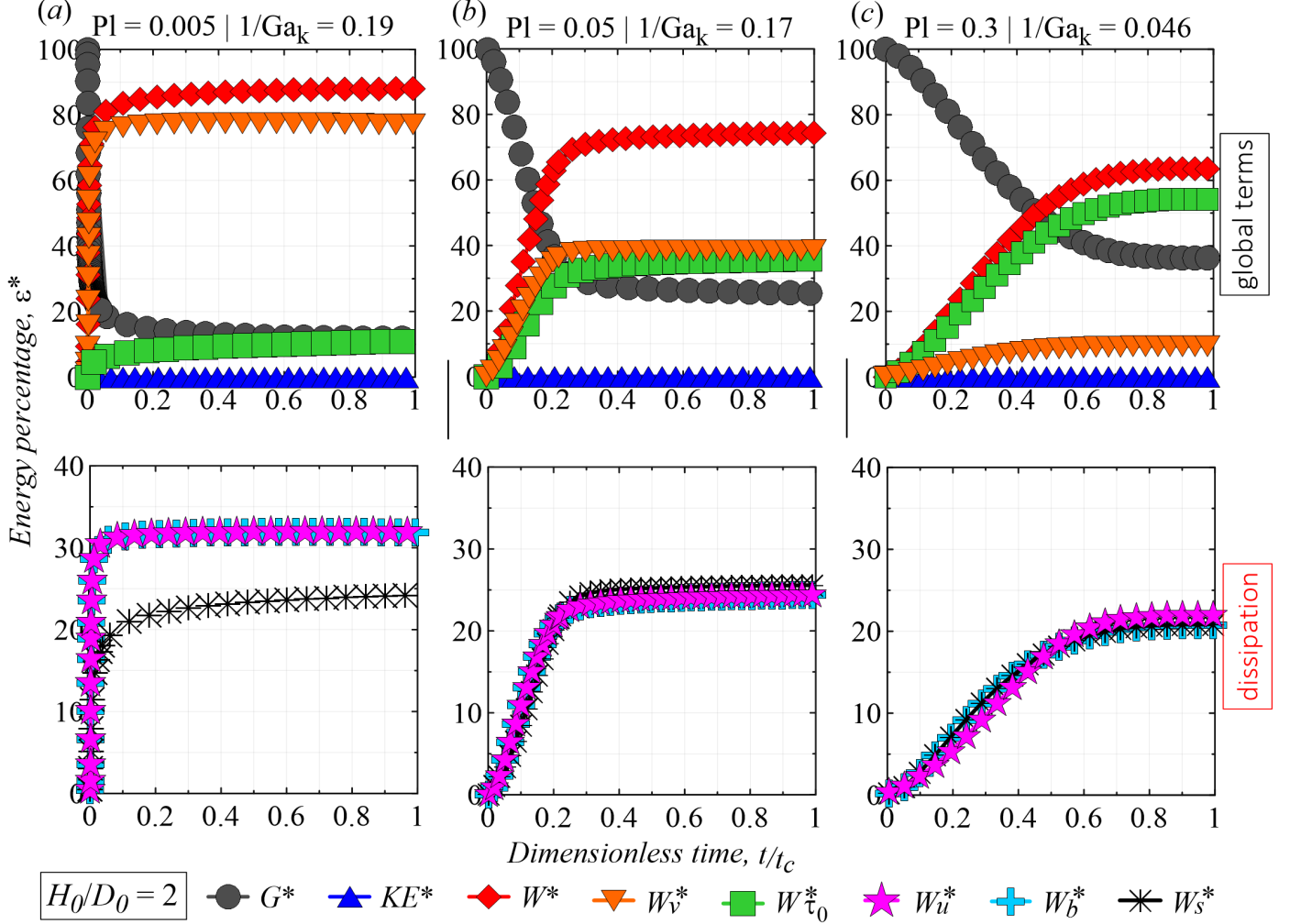


FIG. 4. The energy percentage ϵ^* during the collapse and spreading of viscoplastic elliptical objects with $H_0/D_0 = 2$ is presented for three different $PI-1/Ga_k$ pairs: (a) $PI = 0.005$, $1/Ga_k = 0.19$; (b) $PI = 0.05$, $1/Ga_k = 0.17$; and (c) $PI = 0.3$, $1/Ga_k = 0.046$.

the collapse number $(\frac{1}{PI})^{1/2} \left(\frac{1}{Ga_k}\right)^{1/3} \left(\frac{H_0}{D_0}\right)^{1/6}$. The results reveal a consistent trend line that can be categorised into three distinct regions: (I) the blue region, which corresponds to the gravito-plastic regime where $\frac{D_{max}}{D_0} \sim \left(\frac{1}{PI} \frac{H_0}{D_0}\right)^{1/2}$ (blue dash-dotted line); (II) the red region, associated with the gravito-viscous regime, where $\frac{D_{max}}{D_0} \sim \left(Ga_k \frac{H_0}{D_0}\right)^{1/3}$ (magenta dotted line); and (III) the white region, representing a mixed gravito-visco-plastic regime for which the gravitational, viscous and yield stresses all play a significant role (in this case, $W_v^* \approx W_{\tau_0}^*$ as indicated in sub-figure 4b; $1 \lesssim Co \lesssim 10$).

The rescaled collapse time $\frac{t_c(U_c/H_0)}{(Ga_k H_0/D_0)^{1/3}}$ is plotted in sub-figure 5(b) as a function of Co . The collapse time is approximated as $t_c \sim (H_0 - H_{min})/U_c$, which allows us to write that $t_c(U_c/H_0) \sim (1 - H_{min}/H_0)$. As a result, we find that $t_c(U_c/H_0)$ is a function of H_{min}/H_0 , which in turn is a function Co since $H_{min}/H_0 \sim D_0/D_{max}$ by

mass conservation. Consequently, $t_c(U_c/H_0)$ is a function of Co , as pointed out by sub-figure 5(b) where the numerical data collapse across a master curve.

Lastly, it is essential to emphasize that the new scaling laws presented here are different from those previously reported in the literature using cylindrical and prismatic columns [for which D_{max}/D_0 scales with $(Ga_k \frac{H_0}{D_0})^{1/5}$ in the gravito-viscous regime and $(\frac{1}{PI} \frac{H_0}{D_0})^{1/3}$ in the gravito-plastic regime; 2]. Rationally, these differences emerge from the two-dimensional nature of our flow cases, which ultimately affects the dissipative mechanism within the collapsing objects. In other words, axisymmetric-based scaling laws are not able to predict both the maximum spreading and the collapsing time related to the dam break of the 2D viscoplastic columns. These differences, therefore, allow us to assume the existence of a change in scaling laws induced by the transition from 3D-like to 2D-like objects. However, this transition remains to be

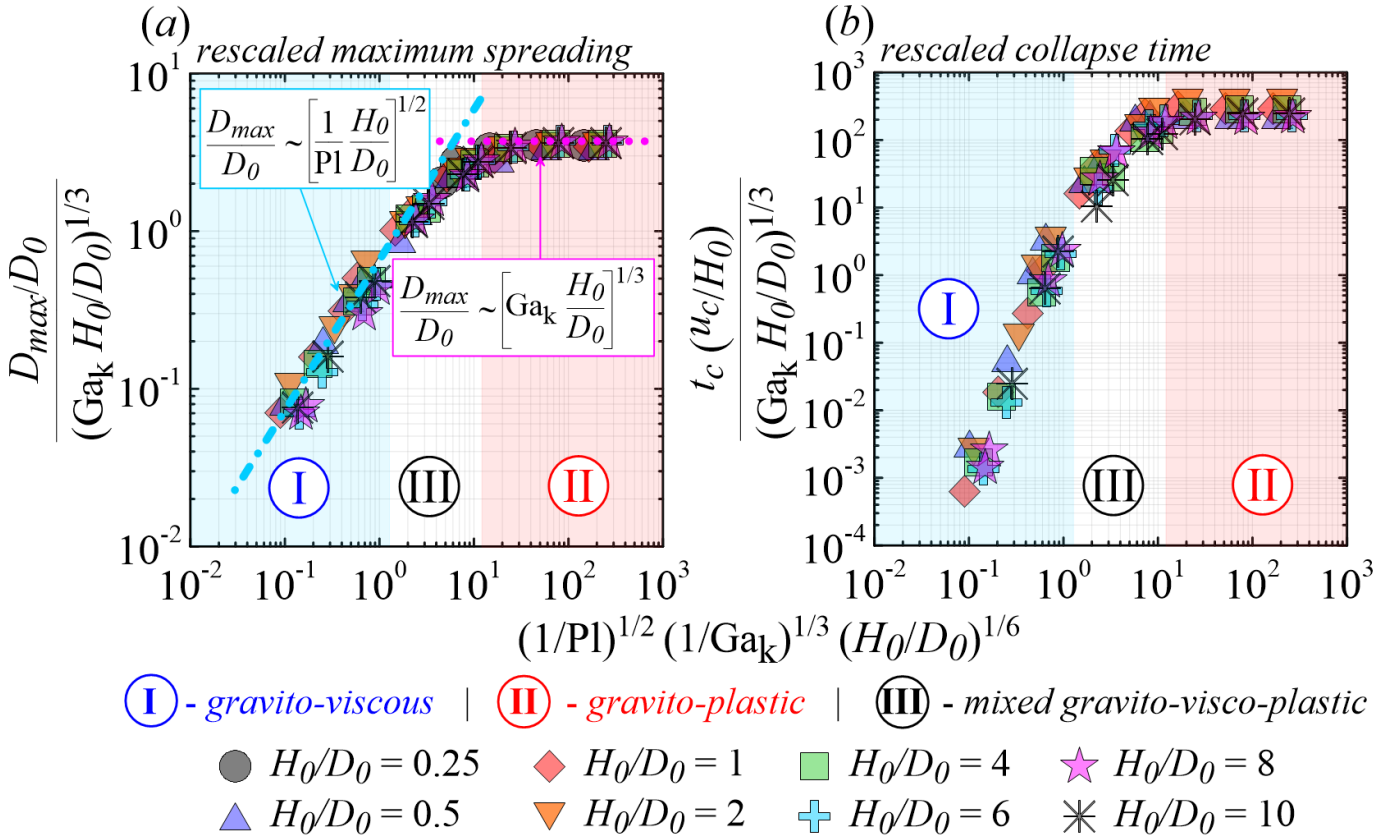


FIG. 5. (a) Rescaled maximum spreading $\frac{D_{max}/D_0}{(Ga_k H_0/D_0)^{1/3}}$ plotted against the collapse number $(\frac{1}{Pl})^{1/2} (\frac{1}{Ga_k})^{1/3} (\frac{H_0}{D_0})^{1/6}$. (b) Rescaled collapsing time $\frac{t_c (u_c/H_0)}{(Ga_k H_0/D_0)^{1/3}}$ against the collapse number. The numerical data align along a master curve that is divided three distinct regions: (I) the blue zone, which corresponds to the gravito-plastic regime; (II) the red zone, which is associated to the gravito-viscous regime; and (III) the white zone, indicating a mixed gravito-visco-plastic regime. Each symbol is associated with an aspect ratio.

studied in depth in future works.

IV. CONCLUDING REMARKS

In this short communication, we have presented a theoretical and numerical study devoted to the physical mechanisms driving the dam break of viscoplastic elliptical columns on a sticky solid (absence of sliding) under gravity effects. Our 2D numerical simulations were based on a variational multi-scale approach dedicated to non-Newtonian multiphase flows. The results obtained were analyzed considering the spreading dynamics, energy balances and new scaling laws.

Three collapse regimes have been highlighted: the gravito-viscous regime, resulting from a competition between gravitational and viscous stresses, for which D_{max}/D_0 scales with $(Ga_k \frac{H_0}{D_0})^{1/3}$; the gravito-plastic regime, resulting from a balance between gravitational and yield stresses, for which D_{max}/D_0 scales with $(\frac{1}{Pl} \frac{H_0}{D_0})^{1/2}$; and the mixed inertio-visco-plastic regime,

for which inertial, viscous and yield stresses are all important. These results were synthesized in the form of a master curve giving the maximum spreading of viscoplastic elliptical objects as a function of a unique dimensionless number called collapse number $Co = (\frac{1}{Pl})^{1/2} (\frac{1}{Ga_k})^{1/3} (\frac{H_0}{D_0})^{1/6}$ relating the three important dimensionless parameters of the problem, namely Ga_k , Pl and H_0/D_0 . The collapse time appears as a function of Co . Interestingly, regardless of the collapsing regime, the explored 2D dam breaks undergo a complex dissipative process emerging from equivalent planar compression/expansion-based and shear-based contributions.

The scaling laws presented here for elliptical objects being different from those associated with the collapse of cylindrical and prismatic viscoplastic columns [2], it would be interesting to analyze in future works the physical mechanisms dominating the spreading transition of objects from 3D to 2D (3D-to-2D transition). Finally, it would also be interesting to incorporate other sources of complexities, including thixotropy, elasticity, inertia, surface tension and slip laws.

Acknowledgements: The authors would like to acknowledge the support from the UCA^{JEDI} program (IDEX of Université Côte d’Azur), the PSL Research University under the program ‘Investissements d’Avenir’ launched by the French Government and implemented

by the French National Research Agency (ANR) with the reference ANR-10-IDEX-0001-02 PSL, and the ANR for supporting the INNpact project under the ‘Jeunes chercheuses et jeunes chercheurs’ program.

-
- [1] Y. Liu, N. J. Balmforth, and S. Hormozi, Axisymmetric viscoplastic dambreaks and the slump test, *Journal of Non-Newtonian Fluid Mechanics* **258**, 45 (2018).
- [2] R. Valette, A. Pereira, S. Riber, L. Sardo, A. Larcher, and E. Hachem, Viscoplastic dam-breaks, *Journal of Non-Newtonian Fluid Mechanics* **287**, 1 (2021).
- [3] N. Pashias, D. V. Boger, J. Summers, and D. J. Glenister, A fifty cent rheometer for yield stress measurement, *Journal of Rheology* **40**, 1179 (1996).
- [4] W. R. Schowalter and G. Christensen, Toward a rationalization of the slump test for fresh concrete: Comparisons of calculations and experiments, *Journal of Rheology* **42**, 865 (1998).
- [5] N. Roussel and P. Coussot, Fifty-cent rheometer for yield stress measurements: from slump to spreading flow, *International Journal of Mineral Processing* **43**, 705 (2005).
- [6] N. J. Balmforth, R. V. Craster, P. Perona, A. C. Rust, and R. Sassi, Viscoplastic dam breaks and the Bostwick consistometer, *Journal of Non-Newtonian Fluid Mechanics* **142**, 63 (2007).
- [7] N. J. Balmforth, I. Frigaard, and G. Ovarlez, Yielding to stress: recent developments in viscoplastic fluid mechanics, *Annual Review of Fluid Mechanics* **46**, 121 (2014).
- [8] E. C. Bingham, An investigation of the law of plastic flows, *Bulletin of the Bureau of Standards* **13**, 309 (1916).
- [9] E. C. Bingham, *Fluidity and plasticity*, McGraw-Hill, New York (1922).
- [10] P. Coussot, Rheophysics of pastes: a review of microscopic modelling approaches, *Soft Matter* **3**, 528 (2007).
- [11] S. Cohen-Addad, H. Reinhard, and O. Pitois, Flow in foams and flowing foams, *Annual Review of Fluid Mechanics* **45**, 241 (2013).
- [12] K. Isukwem, G. Godefroid, C. Monteux, D. Bouttes, R. Castellani, E. Hachem, R. Valette, and A. Pereira, The role of viscoplastic drop shape in impact, *Journal of Fluid Mechanics* **978**, A1 (2024).
- [13] Y. Liu, N. J. Balmforth, S. Hormozi, and D. R. Hewitt, Two-dimensional viscoplastic dambreaks, *Journal of Non-Newtonian Fluid Mechanics* **238**, 65 (2016).
- [14] R. Valette, E. Hachem, M. Khalloufi, A. Pereira, M. R. Mackley, and S. A. Butler, The effect of viscosity, yield stress, and surface tension on the deformation and breakup profiles of fluid filaments stretched at very high velocities, *Journal of Non-Newtonian Fluid Mechanics* **263**, 130 (2019).
- [15] A. Pereira, A. Larcher, E. Hachem, and R. Valette, Capillary, viscous, and geometrical effects on the buckling of power-law fluid filaments under compression stresses, *Computers and Fluids* **190**, 514 (2019).
- [16] A. Pereira, E. Hachem, and R. Valette, Inertia-dominated coiling instabilities of power-law fluids, *Journal of Non-Newtonian Fluid Mechanics* **282**, 104321 (2020).
- [17] K. Isukwem, R. Nemer, E. Hachem, and A. Pereira, Viscoplastic elliptical objects impacting a solid surface, *Physics of Fluids* **36**, 033125 (2024).
- [18] K. Isukwem, C.-A. Charles, T. Phou, L. Ramos, C. Ligoure, E. Hachem, and A. Pereira, Inverse Leidenfrost impacting drops, under consideration for *Journal of Fluid Mechanics*, 1 (2024).
- [19] K. Isukwem, E. Hachem, and A. Pereira, Etude théorique et numérique sur l’étalement d’objets viscoplastiques bidimensionnels impactant une surface solide, *Rhéologie* **45**, 35 (2024).
- [20] T. C. Papanastasiou, Flows of materials with yield, *Journal of Rheology* **31**, 385 (1987).